





Article

CO Total and Preferential Oxidation over Stable Au/TiO₂ Catalysts Derived from Preformed Au Nanoparticles

Núria J. Divins ^{1,*} , Eduardo López ², Inmaculada Angurell ³ , Stefan Neuberg ⁴, Ralf Zapf ⁴, Gunther Kolb ⁴  and Jordi Llorca ^{1,*} 

¹ Institute of Energy Technologies, Department of Chemical Engineering and Barcelona Research Centre in Multiscale Science and Engineering, Universitat Politècnica de Catalunya, Campus EEBE, Eduard Maristany 10-14, 08019 Barcelona, Spain

² Planta Piloto de Ingeniería Química, PLAPIQUI (UNS-CONICET), Camino la Carrindanga Km 7, 8000 Bahía Blanca, Argentina; elopez@plapiqui.edu.ar

³ Department of Inorganic and Organic Chemistry, Inorganic Chemistry Section, Universitat de Barcelona, Martí i Franquès 1, 08028 Barcelona, Spain; inmaculada.angurell@qi.ub.es

⁴ Fraunhofer Institute of Microengineering and Microsystems, Carl-Zeiss-Str. 18-20, D-55129 Mainz, Germany; Stefan.Neuberg@imm.fraunhofer.de (S.N.); Ralf.Zapf@imm.fraunhofer.de (R.Z.); gunther.kolb@imm.fraunhofer.de (G.K.)

* Correspondence: nuria.jimenez.divins@upc.edu (N.J.D.); jordi.llerca@upc.edu (J.L.)

Received: 29 July 2020; Accepted: 1 September 2020; Published: 7 September 2020



Abstract: CO preferential oxidation (PROX) is an effective method to clean reformat H₂ streams to feed low-temperature fuel cells. In this work, the PROX and CO oxidation reactions were studied on preformed Au nanoparticles (NPs) supported on TiO₂ anatase. Preformed Au NPs were obtained from gold cores stabilized by dodecanethiols or trimethylsilane-dendrons. A well-controlled size of ca. 2.6 nm and narrow size distributions were achieved by this procedure. The catalysts were characterized by high-resolution transmission electron microscopy and ex situ and in situ X-ray photoelectron spectroscopy (XPS). The XPS results showed that the preformed Au NPs exhibited high thermal stability. The different ligand-derived Au catalysts, as well as a conventional gold catalyst for comparison purposes, were loaded onto cordierite supports with 400 cells per square inch. The activity and selectivity of the samples were evaluated for various operation conditions. The catalyst prepared using dodecanethiol-capped Au NPs showed the best performance. In fact, CO conversions of up to 70% at 40% CO₂ selectivity and 90% O₂ conversion were observed operating at 363 K in H₂-rich atmospheres. The performance of the best catalysts was subsequently tested on stainless steel microreactors. A 500-hour stability test was carried out under a real post-reformat stream, including 18 vol.% CO₂ and 29 vol.% H₂O. A mean CO conversion of ca. 24% was measured for the whole test operating at 453 K and a gas hourly space velocity (GHSV) of 1.3 × 10⁴ h⁻¹. These results reveal our dodecanethiol- and carbosilane-derived Au catalysts as extremely promising candidates to conduct a PROX reaction while avoiding deactivation, which is one of the major drawbacks of Au/TiO₂ catalysts.

Keywords: preformed Au nanoparticles; dendrons; dendrimers; thiols; CO oxidation; PROX; CO-PrOx; microreactor; fuel reformer; stability test

1. Introduction

The depletion of fossil fuels and the growing demands for cleaner and renewable energy made hydrogen and fuel cells (FC) appear as valuable technologies for new energy management. Hydrogen

is usually produced from the reforming of hydrocarbons or alcohols, leading to H₂ streams that contain high amounts of CO, CO₂, and H₂O [1,2]. CO is also a pollutant and is heavily toxic. Therefore, an important aspect of FC technology is fuel processing. Consequently, developing processes devoted to obtaining CO-free H₂ streams is an essential requirement for mobile energy production or portable systems, where proton exchange membrane FCs (PEMFCs) are chosen [3]. In particular, to feed low temperature PEMFCs, the CO concentration should be reduced to values below ca. 10 ppm to avoid Pt anode poisoning [4]. In this regard, CO preferential oxidation (PROX) reaction is an appealing and efficient method to selectively oxidize the CO (ca. 1–2 vol.%) still present in pre-cleaned reformat streams to levels below 10 ppm, while avoiding the oxidation of H₂ (concentration between 40–70%) to minimize fuel losses, in the temperature range 353–473 K [5,6]. Thus, highly selective catalysts towards CO₂ are required.

Many catalytic formulations have been tested to find a suitable catalyst design to competitively oxidize CO in the presence of H₂, which, according to the active metal selected, can be organized into three categories [5,7]: (i) Pt group metals, mainly Pt, Ru, Rh, Pd, and Ir; (ii) transition metals, such as Cu, and (iii) Au-based catalysts. Among them, Au-supported catalysts have shown exceptionally high activity for CO oxidation at low temperatures when Au is dispersed as nanoparticles smaller than 5 nm [8].

Several critical factors determine the exceptional catalytic nature of Au-supported catalysts. In some cases, they are intimately related, such as the gold particle size, morphology, and oxidation state, the metal oxide support chosen and its crystalline structure, the architecture of the Au-support interaction, and/or the presence of promoters [8–12]. In particular, it has been shown that the size of Au nanoparticles (NPs) plays a crucial role in their exceptional catalytic activity. It has been observed that Au NPs 2–4 nm in diameter exhibited two orders of magnitude higher CO oxidation rates than 20–30 nm NPs [12]. Furthermore, it has been reported that for Au NPs of diameters above 6–10 nm, their catalytic activity is particularly lost and 9-nm NPs are almost inactive for CO oxidation [13]. Under reaction conditions, Au NPs easily sinter and highly dispersed small Au NPs will eventually evolve to larger particles, which are thermodynamically more favorable [14]. Therefore, one of the main drawbacks of Au-based catalysts is their deactivation in long-term operation [5,15]. This requires the development of extremely thermally stable Au NPs under reaction conditions.

Several synthesis approaches have been investigated to synthesize Au NPs supported on metal oxides, such as impregnation methods, co-precipitation, hydrothermal, adsorption, deposition–precipitation, organic capping, and micelle and dendrimer encapsulation, among others. In contrast to impregnation methods, the use of organic capping and encapsulation methods allows the synthesis of NPs with a controlled and well-defined size, which is determined before deposition on the metal oxide support [13,16,17]. Moreover, in these methods, the presence of coordinating ligands prevents the aggregation of the NPs and tunes the interface between the NP and the support [18,19].

Another important aspect of the PROX reaction is the reactor design, which, together with an active catalyst, is required to bring CO levels to below 50 ppm [20]. The reactor design plays a key role in eliminating the heat released by the oxidation reactions of H₂ and CO from the reaction medium to preserve appropriate selectivity towards CO₂. In this context, microreactors appear as valuable devices to achieve this due to their distinctive features, such as high surface-to volume ratios and thin catalytic coatings in direct contact with the channels' walls, which result in superior heat and mass transfer rates than in conventional packed-bed reactors [20–22].

In this work, we investigated the thermal stability of preformed Au NPs and the role of the gold–metal oxide interface. To this end, we synthesized well-defined Au cores of ca. 3 nm encapsulated in different generations of trimethylsilane (TMS) dendrons and dodecanethiols, which are radially bound to the Au cores (nanoparticle-cored dendrimers, Au@NCD). The preformed Au NPs were supported on TiO₂, as Au/TiO₂ catalysts have been considered as one of the most active systems for the PROX reaction [23,24]. We characterized the developed catalysts by high-resolution transmission electron microscopy (HRTEM) and in situ X-ray photoelectron spectroscopy (XPS). Finally,

we evaluated the catalytic performance of the developed materials for CO oxidation and PROX reactions, studying mixtures containing up to 50 vol.% H₂, on different structured catalysts. We started the catalytic screening of the preformed Au-based catalysts using conventional cordierite monoliths and, subsequently, we also used stainless steel microreactors to profit from their improved thermal management. Our evaluations concluded with 500-h stability tests under a reformat surrogate stream, containing 18 vol.% CO₂ and 29 vol.% steam, performed on microreactors, to investigate the stability of the preformed Au NPs under real PROX reaction conditions. The results showed that our dodecanethiol- and carbosilane-derived Au catalysts are extremely stable and, thus, promising candidates to conduct a PROX reaction and avoid deactivation.

2. Results and Discussion

2.1. Morphological and Structural Properties of the Preformed Au@NCD and Au@NCD/TiO₂ Catalysts

2.1.1. TEM Characterization of Unsupported Au@NCD

The preformed and unsupported Au NPs encapsulated on the different organic shells were studied by TEM. Low-magnification TEM images are shown in the first two columns of Figure 1, where well-dispersed Au cores with homogeneous size distribution encapsulated on dodecanethiols and the different generations of dendrons (Au@D, Au@G0, Au@G1, and Au@G2, respectively) are visible (see the Materials and Methods section and Table 1 for details on the nomenclature used for the Au NPs). Analysis of the Au cores diameters renders a size distribution for Au@G0 of 2.7 ± 0.8 nm, for Au@G1 of 2.5 ± 0.7 nm, for Au@G2 of 2.6 ± 0.6 nm, and 1.8 ± 0.6 nm for the Au@D cores. These results show that the synthesis method was successful as narrow size distributions were obtained and the sizes of the Au cores capped with the different organic shells are very similar. Additionally, these results show that a correlation between the Au cores' size and the dendron generation did not exist [25]. The HRTEM images and their corresponding Fourier transform (FT) images allowed for the identification of the Au crystalline structure. In all samples, lattice fringes at 2.36 Å and 2.04 Å were identified, which correspond to (111) and (200) crystallographic planes of metallic Au face-centered cubic (fcc), respectively.

Table 1. Nomenclature of the gold nanoparticles.

| Name | Gold Precursor | Ligands |
|-------|---------------------------------------|------------------------|
| Au@D | Preformed Au@D NPs | Dodecanethiols |
| Au@G0 | Preformed Au@G0 NPs | G0 generation dendrons |
| Au@G1 | Preformed Au@G1 NPs | G1 generation dendrons |
| Au@G2 | Preformed Au@G2 NPs | G2 generation dendrons |
| AuC | HAuCl ₄ ·3H ₂ O | None |

2.1.2. Characterization of TiO₂

The crystalline structure of TiO₂ synthesized from Ti^{IV} isopropoxide was investigated by X-ray diffraction (XRD). The diffractogram showed peaks corresponding to interplanar distances (d_{hkl}) 3.52 Å, 2.38 Å, 1.89 Å, 1.70 Å, 1.67 Å and 1.48 Å, respectively, which correspond to TiO₂ anatase, indicating that the anatase TiO₂ polymorph forms under the calcination conditions chosen. A Brunauer–Emmett–Teller (BET) surface area of 264 ± 1 m²/g and an average pore diameter of 3.9 nm were obtained.

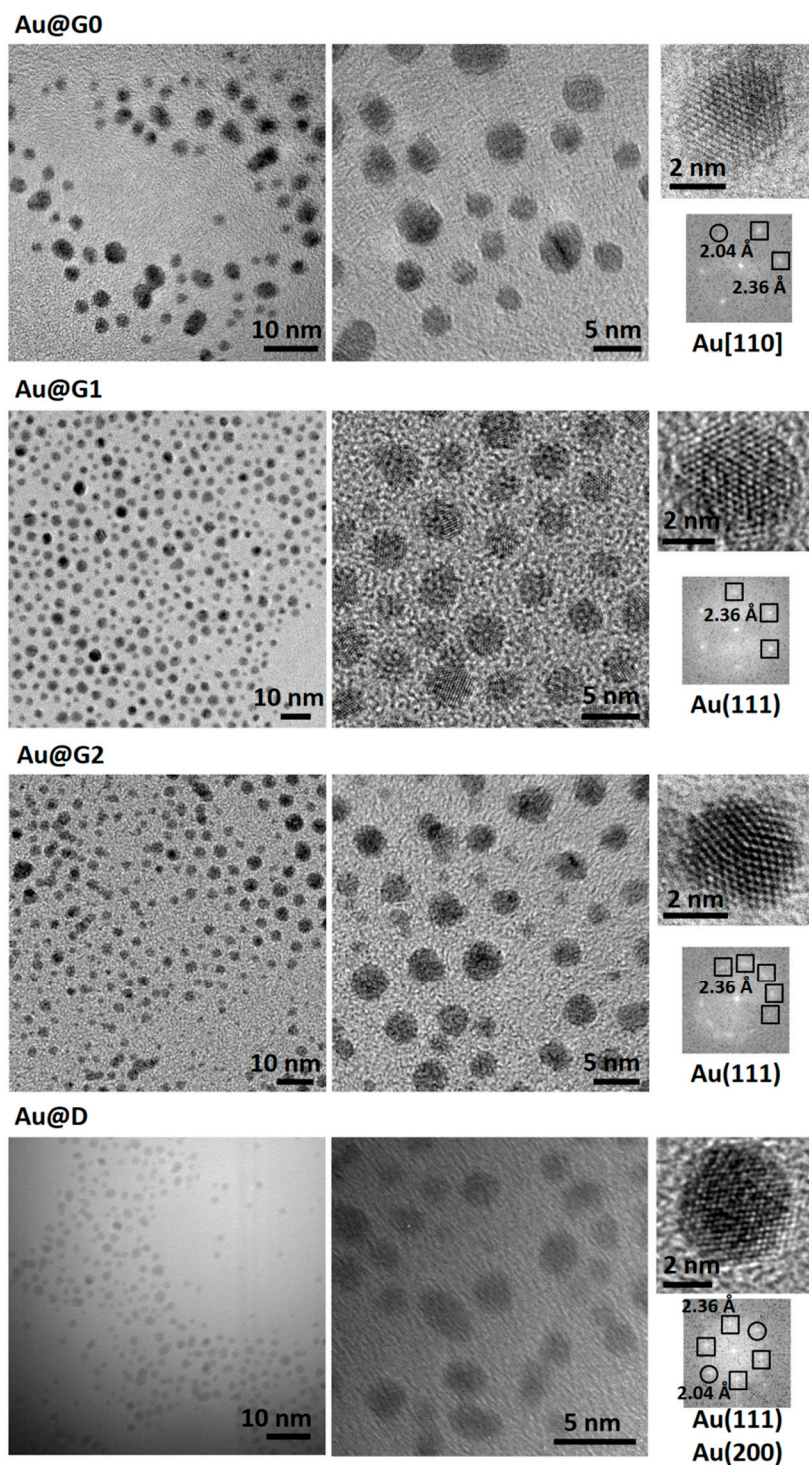


Figure 1. TEM images of the unsupported ligand-protected core-shell Au nanoparticles (NPs) acquired at different magnifications.

2.1.3. TEM Characterization of Au/TiO₂ Catalysts

Representative TEM images of Au@G1/TiO₂ and of a catalyst prepared using a conventional salt precursor (HAuCl₄·3H₂O) (see Materials and Methods section and Table 1 for the synthesis details), the AuC/TiO₂ catalyst, are shown in Figure 2. For TEM analyses, the catalyst Au@G1/TiO₂ was chosen as representative of the dendron-protected Au NPs and the images were compared to those obtained on a conventional catalyst. A general view in low-magnification mode of Au@G1 NPs supported on

TiO₂ after calcination at 673 K is shown in Figure 2a. The Au@G1 NPs were found to be well-dispersed over the TiO₂ support and their mean particle size increased to 5.1 ± 1.2 nm, due to the calcination performed at 673 K; nevertheless, they kept a narrow size distribution. Figure 2b,c show HRTEM images of representative Au@G1 NPs in intimate contact with TiO₂. The lattice fringes exhibited by Au@G1/TiO₂ correspond to TiO₂ anatase and to (111) crystallographic planes of Au fcc. HRTEM images of the AuC/TiO₂ reference catalyst calcined at 723 K are shown in Figure 2d–g. Gold NPs in close contact with TiO₂ are distinguished via HRTEM imaging of AuC/TiO₂. An analysis of the FT images revealed that Au is present in the Au fcc structure as well. The size distribution was 3.6 ± 1.2 nm.

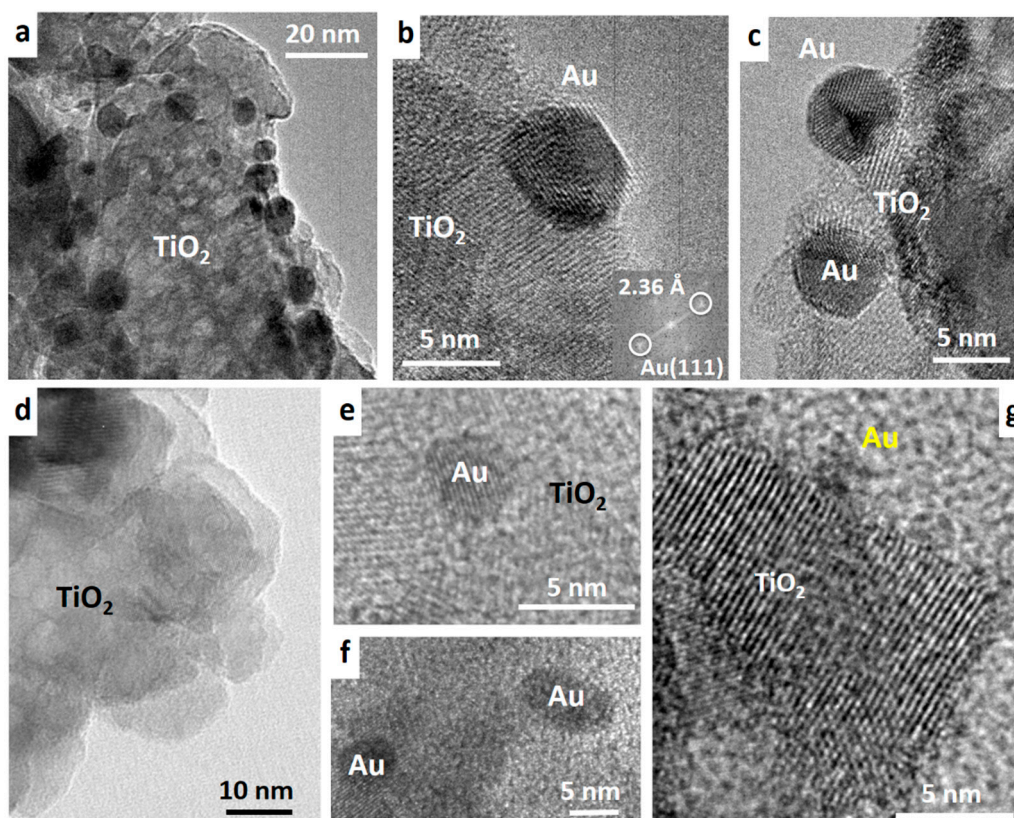


Figure 2. TEM images of (a–c) Au@G1/TiO₂ catalyst calcined at 673 K and (d–g) AuC/TiO₂ catalyst calcined at 723 K. (b,c) Detailed high-resolution transmission electron microscopy (HRTEM) images of individual Au@G1 NPs anchored to a TiO₂ crystallite. The corresponding FT image is shown in the inset in (b). (e–g) Detailed HRTEM image of individual AuC NPs anchored to TiO₂.

2.2. In Situ XPS Studies: Thermal Stability of Au@NCD/TiO₂ Catalysts and Surface Reorganization

A successful synthesis of Au NPs encapsulated in dodecanethiols and different generations of dendron shells was demonstrated by TEM analyses. Therefore, the developed Au@NCD proved to be appropriate for the achievement of Au nanostructured materials owing to its monodispersity and size control. Nevertheless, the catalytic properties of the preformed gold cores, including reactant accessibility and deactivation by particle sintering, had to be properly addressed. Thus, XPS analyses were carried out to investigate the ease of removing the encapsulating organic shells and the sintering propensity of TiO₂-supported Au@D, Au@G1, and Au@G2 NPs. Silicon wafers were loaded with the different Au@NCD/TiO₂ catalysts and annealed in an ultra-high vacuum (UHV) directly inside the analysis chamber of the XPS system. The sequence of treatments consisted of annealing at: (i) 398 K, (ii) 523 K, (iii) 598 K, (iv) 673, and (v) 773 K. Table 2 lists the Au/C atomic ratios obtained for each treatment.

Table 2. XPS results of the annealing treatments under ultra-high vacuum (UHV) at the indicated temperatures for Au@D/TiO₂, Au@G1/TiO₂, and Au@G2/TiO₂ catalysts.

| Temperature (K) | Au/C (Atomic Ratio × 100) | | |
|-----------------|---------------------------|------------------------|------------------------|
| | Au@D/TiO ₂ | Au@G1/TiO ₂ | Au@G2/TiO ₂ |
| As-synthesized | 25.6 | 6.8 | 0.6 |
| 398 | 44.8 | 7.9 | 2.6 |
| 523 | 43.5 | 9.5 | 5.1 |
| 598 | 40.0 | 12.5 | 9.1 |
| 673 | 41.9 | 17.9 | 10.4 |
| 773 | 41.0 | 13.8 | 8.1 |

As expected, the as-prepared Au@D/TiO₂ showed the highest Au/C atomic ratio, while the lowest was found for Au@G2/TiO₂, as the encapsulating shell contains the highest amount of C atoms. This ratio increased for the successive annealing treatments following the order: Au@D/TiO₂ > Au@G1/TiO₂ > Au@G2/TiO₂. For Au@G1/TiO₂ and Au@G2/TiO₂, the Au/C ratio progressively increased as the temperature increased up to 673 K, indicating that the dendron shell was gradually removed as the temperature increased. It is noteworthy that for Au@D/TiO₂ the same trend was observed up to 523 K, revealing that dodecanethiols can be removed at lower temperatures than dendrons. For higher temperatures (≥598 K), the Au/C ratio stabilized for Au@D/TiO₂, probably indicating that minor removal of the dodecanethiol shell still took place together with mild sintering of the Au cores. On the other hand, the Au/C ratio decreased for Au@G1/TiO₂ and Au@G2/TiO₂ at 773 K. This implies a decrease in the Au surface signal, and thus suggests that some sintering of the Au cores took place. Au@G1 and Au@G2 NPs showed similar losses of organic ligands at each temperature step, whereas the loss of dodecanethiol ligands was remarkably higher. Large quantities of carbon remained on the catalysts' surface at 773 K, which we ascribed to the performance of the experiments under UHV conditions, and thus without the presence of a gaseous atmosphere able to drag the organic residues. Therefore, the trends for the three catalysts have to be considered and not the absolute values.

The dendrons' removal and the surface reorganization were further investigated by XPS on an Au@G0/TiO₂ pellet. This consisted of the performance of a sequence of in situ treatments in a high-pressure cell directly connected to the XPS analysis system. The sequence included oxidation treatments as well as a PROX experiment (see details in the Materials and Methods section). The surface atomic ratios determined by XPS are listed in Table 3 and Au 4f and Ti 2p spectral regions are shown in Figure 3. After each oxidation step, a slight decrease in the Au/Ti ratio occurred, indicating a slight agglomeration of the Au@G0 NPs. In parallel, up to 673 K the Au/C ratio gradually increased after each oxidation step. A large increase in the Au/C ratio was observed after the oxidation at 673 K, denoting that the organic shell was removed to a larger extent than in the previous steps. This is in line with the results obtained under UHV for Au@G1/TiO₂ deposited on a Si wafer. For the series of in situ treatments, the presence of an airstream facilitated the removal of the encapsulating organic dendrons, leading to remarkably higher Au/C ratios than for the previous experiments performed under UHV.

Table 3. Surface atomic ratios determined by XPS for the in situ sequence performed inside the high-pressure cell for the Au@G0/TiO₂ pellet.

| Treatment | Atomic Ratio × 100 | | | |
|-----------------------|--------------------|-------|-------|-------|
| | Au/C | Au/Ti | Si/Ti | Si/Au |
| 1. As-synthesized | 48 | 38 | 82 | 215 |
| 2. Oxidation at 473 K | 55 | 34 | 78 | 227 |
| 3. Oxidation at 573 K | 65 | 30 | 78 | 261 |
| 4. Oxidation at 673 K | 129 | 29 | 39 | 133 |
| 5. PROX at 673 K | 296 | 29 | 44 | 154 |
| 6. Oxidation at 773 K | 239 | 27 | 58 | 220 |
| 7. Oxidation at 873 K | 289 | 26 | 363 | 1389 |

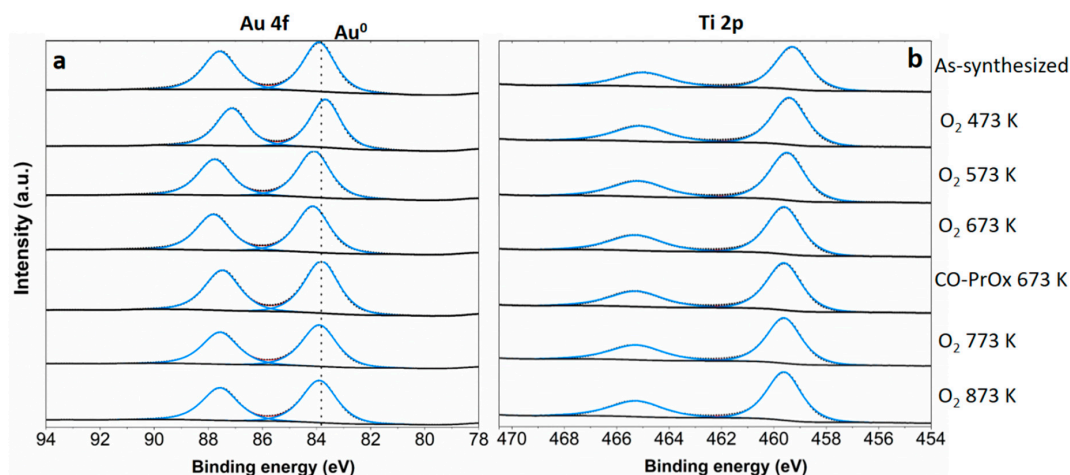


Figure 3. XPS spectra of Au@G0/TiO₂ acquired during the in situ series after the treatments (gases and temperatures) indicated on the plot. (a) Au 4f, (b) Ti 2p spectral regions.

Interestingly, after the PROX test (3 mL/min CO + 3 mL/min H₂ + 15 mL/min air – mixture B-like conditions, see Materials and Methods section), at 673 K, the Au/C experienced its largest increment, reaching its highest value, while Si/Au reached one of its lower values. Therefore, the reaction atmosphere enhances the removal of dendrons and promotes the segregation of Au towards the surface of the core–shell NPs, causing a larger restructuring of the surface than the oxygen atmosphere at the same temperature (673 K). Au/Ti and Au/C ratios experienced minor changes after the subsequent calcinations at 773 and 873 K, evidencing the removal of the organic shell during the previous steps and mostly in the course of the PROX reaction. On the other hand, Si/Au and Si/Ti ratios increased significantly after the oxidation at 873 K, showing that the dendrons’ residues (mostly SiO₂) covered part of the Au@G0/TiO₂ catalyst. As reported in [18], the Si that initially forms the dendrons is progressively converted to SiO₂ upon oxidation, resulting in a ligand-assisted pinning mechanism of the Au cores by the SiO₂ derived from the different generations of dendrons. This is schematically represented in Figure 4.

For all the conditions tested, the binding energy of Au 4f electrons was at ca. 84.0 eV, indicating that Au was present in a zero-valence state [26].

2.3. CO Oxidation and PROX Catalytic Tests

2.3.1. On Cordierite Monoliths

Initially, the catalytic performance of the four catalysts derived from preformed Au NPs and of a catalyst prepared using the conventional Au precursor was screened with the catalysts supported on cordierite monoliths. In light of the XPS results, showing that both the oxidations and the catalytic atmosphere removed the encapsulating shell and increased the Au/C ratio; the catalysts derived from preformed Au NPs were first tested as-prepared, i.e., without performing any pretreatment after the synthesis procedure to find the optimum activation treatment. Next, stepwise oxidations were performed after each catalytic cycle. Studying the performance of the catalysts after oxidations done at increasing temperatures allowed for monitoring the effect of the catalytic mixtures and calcination temperatures on the catalytic performance, which can influence not only the removal of the organic shell, but also result in different metal–support interactions and different architectures of the Au–TiO₂ interface [16,18]. The sequence of catalytic experiments is schematically represented in Figure S1. The concentrations of the three mixtures investigated are listed in Table 4.

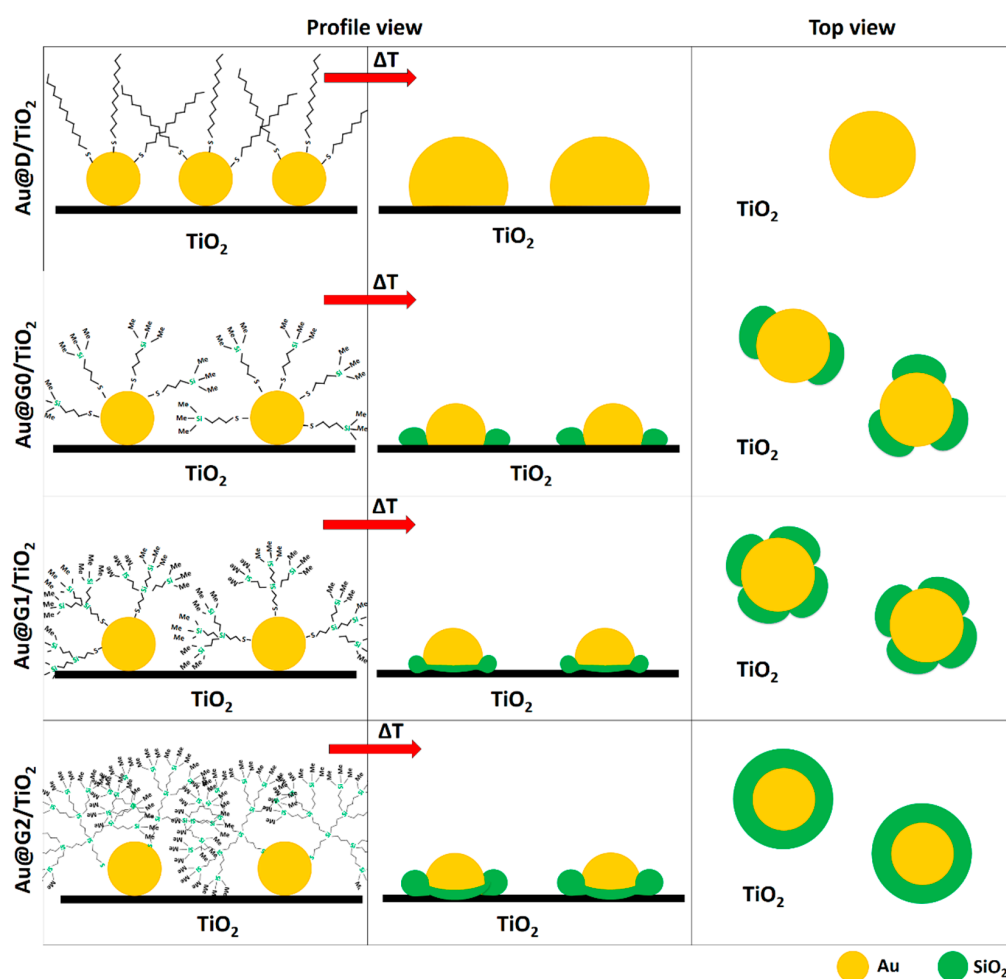


Figure 4. Schematic representation of the ligand-assisted pinning mechanism of Au cores for the different generations of dendrons after thermal treatments.

Table 4. Composition of the inlet mixtures.

| Mixture | Concentration (vol.%) | | | |
|---------|-----------------------|----------------|----------------|----|
| | CO | O ₂ | H ₂ | Ar |
| A | 2 | 2 | 0 | 96 |
| B | 2 | 2 | 2 | 94 |
| C | 2 | 2 | 50 | 46 |

The first catalytic tests were carried out on an as-prepared 2 wt.% Au@D/TiO₂ catalyst. At 363 K under mixture B (2 vol.% CO, 2 vol.% O₂, 2 vol.% H₂, balanced in Ar), the fresh catalyst showed poor catalytic activity, with a CO conversion below 1%, as shown in Figure 5a. Thus, the temperature was directly increased to 473 K. Full CO conversion was obtained at 473 K, together with a selectivity towards CO oxidation of ca. 48%. After 1 h under reaction conditions, the reaction cycle was restarted by lowering the temperature to 363 K. CO conversion decreased slightly ($\chi_{\text{CO}} = 97.3\%$), whereas the selectivity to CO₂ reached $S_{\text{CO}_2} = 76\%$. This demonstrated that dosing mixture B at only 473 K already activated the catalyst and thus created active sites. This is in agreement with the in situ XPS results, which showed that dosing the catalytic mixture enhanced the removal of carbon and decreased the Si/Au ratio. Additionally, the effect of dosing mixture B at higher temperatures can have a similar effect as a prereduction treatment, which has been related to the formation of OH⁻ groups at the support surface or to a partial reduction in the support [27,28].

Following the reaction cycle schematized in Figure S1, the reactant mixture was switched to mixture A (2 vol.% CO, 2 vol.% O₂, balanced in Ar), while Keeping the reaction temperature at 363 K. Under these conditions, total CO conversion was reached (Figure S2). Finally, mixture C (2 vol.% CO, 2 vol.% O₂, 50 vol.% H₂, balanced in Ar) was dosed to evaluate the effect of H₂ concentrations close to those in post-reformate streams. An approximately 65% CO conversion was attained together with S_{CO₂} = 30% (Figure 6a). The reaction cycle continued at 398, 433, and 473 K, and the first oxidation was performed. Remarkably, as seen in Figures 5a and 6a, the catalytic activity of Au@D/TiO₂ was enhanced after the oxidation at 773 K both in terms of S_{CO₂} for mixture B and in χ_{CO} and S_{CO₂} for mixture C. As inferred from the XPS data shown in Table 2, after the oxidation at 673 K, the dodecanethiols' shell was almost completely removed. Therefore, the improvement observed on the catalytic performance after the oxidation at 773 K, rather than after 673 K, may not only be caused by the removal of the organic shell. The formation of a stronger interaction between Au and TiO₂ or a specific architecture of the Au-TiO₂ contact area also play a crucial role in the catalytic phenomenon, as the CO oxidation occurs at the perimeter sites of the Au-TiO₂ interface, as previously reported [29,30]. As reported in Figure 5a, after this oxidation, for mixture B experiments, the catalyst achieved 96% CO conversion with 88% CO₂ selectivity at 363 K. For higher temperatures, total CO oxidation was attained together with a decrease in the CO₂ selectivity, as expected. Even so, not all the oxygen supplied was consumed. These results show a remarkable performance of the Au@D/TiO₂ catalyst, achieving—at 398 K—complete CO oxidation with S_{CO₂} = 73% for mixture B.

For mixture C experiments, due to the competitive oxidation of CO and H₂, the highest CO conversions were recorded for the lowest reaction temperatures (363 K). For instance, after the oxidation at 773 K, χ_{CO} = 68%, χ_{O_2} = 93% and S_{CO₂} = 38% were achieved at 363 K (Figure 6a). Figure S2a reports the CO oxidation tests (mixture A experiments). Complete CO conversion was achieved for all tests, except after oxidation at 773 K, at which point χ_{CO} remained at 94% (at 363 K).

Subsequently, the catalytic performance of the dendron-capped Au NPs and the conventional catalyst (reference catalyst) was evaluated. The experimental results of CO and O₂ conversion, and selectivity to CO₂, are plotted in Figure 5, Figure 6, and Figure S2, for mixtures B, C, and A, respectively. For mixture B studies, contrary to the operation of Au@D/TiO₂, Au@G0/TiO₂ and Au@G1/TiO₂ catalysts only attained total CO oxidation at a high reaction temperature (473 K). Nevertheless, higher CO₂ selectivities were achieved for all the temperatures, including those corresponding to a full CO conversion operation. For Au@G0/TiO₂, at 433 K, without performing any calcination, almost complete CO oxidation was attained (χ_{CO} = 97%, which corresponds to 540 ppm of CO in the outlet stream) with a CO₂ selectivity of 73%. In clear contrast to the operation of Au@D/TiO₂, calcinations at 673 and 773 K had a strong negative effect on the performance of Au@G0/TiO₂ and Au@G1/TiO₂ catalysts. In fact, for Au@G0/TiO₂, after the oxidation at 773 K, the catalytic activity dropped dramatically. This was a surprising effect, as in a previous study [18], Au@G0 NPs supported on SrTiO₃ (STO) showed higher thermal stability and resistance against sintering at higher temperatures than Au@D, also supported on STO. This suggests that, while the carbosilane residues formed upon calcinations acted as pinning centers for gold nuclei, preventing their aggregation, their presence surrounding the Au cores was detrimental to the catalytic performance. Hindering access to the Au-TiO₂ perimeter sites of reactants or a weaker interaction between Au and the TiO₂ support could be responsible for this effect. For mixture C, prior to the calcination at 773 K, Au@G0/TiO₂ exhibited slightly higher CO conversion and CO₂ selectivity at intermediate temperatures (398 and 433 K) than Au@D/TiO₂.

Concerning the catalytic performance of Au@G2/TiO₂, very low catalytic activity was registered for the whole reaction cycle (results shown only for mixture B, Figure 5d). Therefore, to facilitate the removal of the G2 dendron shell, an additional calcination at 873 K was included. Nevertheless, the conversion only reached 5%, demonstrating that Au@G2/TiO₂ was not appropriate for PROX, probably due to the presence of SiO₂ covering the perimeter of the Au NPs.

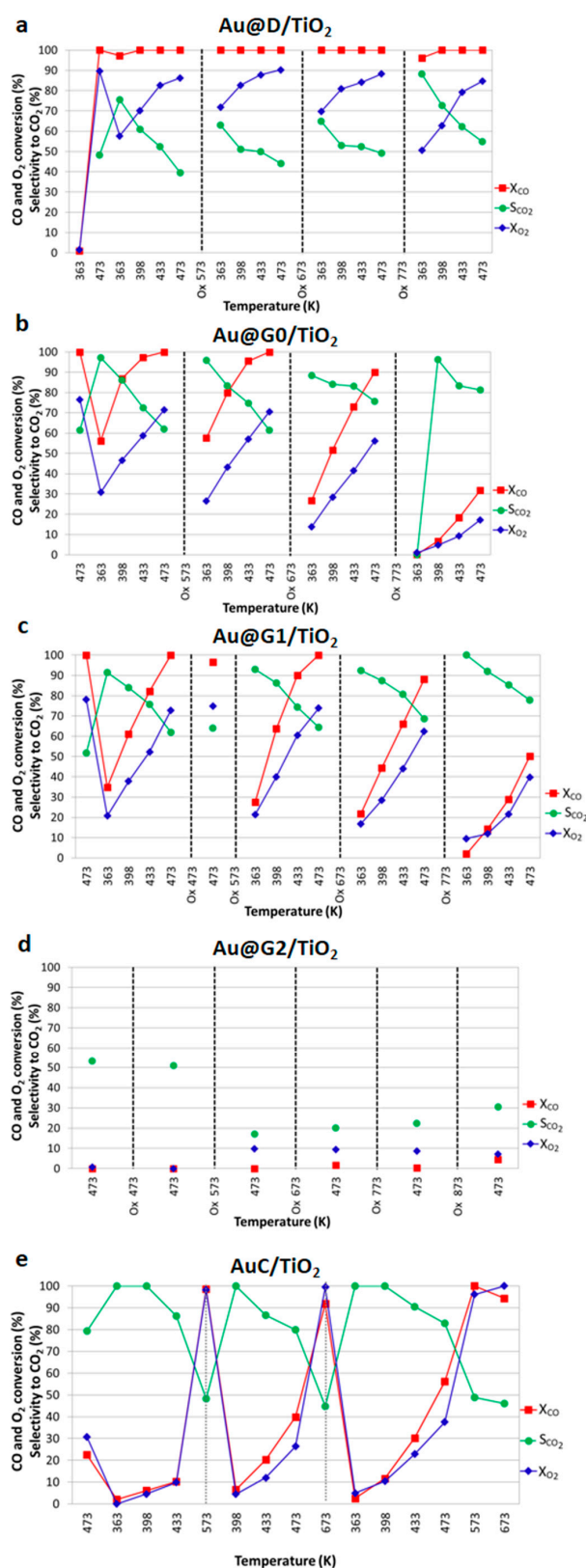


Figure 5. Temperature dependence performance of (a) Au@D/TiO₂, (b) Au@G0/TiO₂, (c) Au@G1/TiO₂, (d) Au@G2/TiO₂, and (e) AuC/TiO₂ catalysts for mixture B (2 vol.% CO, 2 vol.% O₂, 2 vol.% H₂, 94 vol.% Ar). Black vertical lines in (a–d) indicate the oxidations performed; grey lines in (e) show when mixture B was dosed at higher temperature.

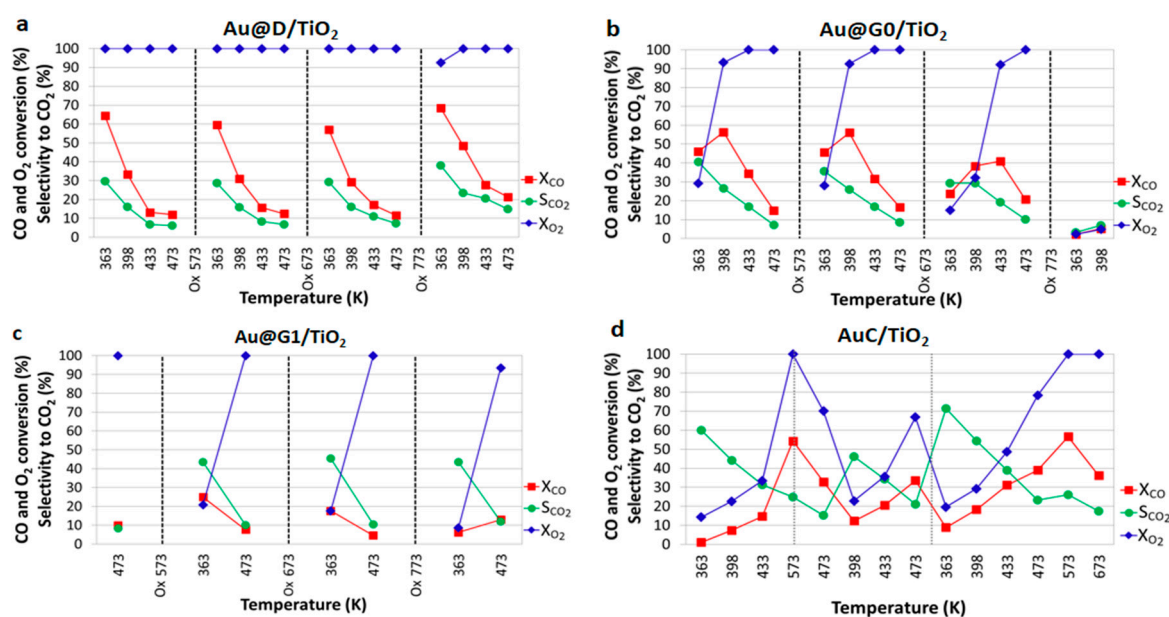


Figure 6. Temperature dependence performance of (a) Au@D/TiO₂, (b) Au@G0/TiO₂, (c) Au@G1/TiO₂, and (d) AuC/TiO₂ catalysts for mixture C (2 vol.% CO, 2 vol.% O₂, 50 vol.% H₂, 46 vol.% Ar). Black vertical lines in (a–c) indicate the oxidations performed; grey lines in (d) show when mixture B was dosed at a higher temperature.

Initially, the conventional AuC/TiO₂ catalyst showed lower catalytic activity than Au@D/TiO₂, with the CO conversion being 20% and the O₂ conversion 30% at 473 K under mixture B (Figure 5e). Next, the catalytic performance at 363, 398, and 433 K was investigated. Nevertheless, at lower temperatures, the activity was lower too. To activate the catalyst, we rose the temperature under mixture B to 573 K and full CO conversion was reached, together with complete H₂ consumption. A minor beneficial influence on the catalytic performance for the three mixtures was observed upon exposure to mixture B at 573 K. Consequently, an additional activation treatment under mixture B was performed at an increasing temperature (673 K), as the catalyst was already calcined at 723 K, and calcination at higher temperatures could lead to Au NPs sintering. The catalytic performance slightly increased again; nonetheless, the catalytic activity of AuC/TiO₂ was markedly lower than that of Au@D/TiO₂, Au@G0/TiO₂, and Au@G1/TiO₂ catalysts.

Consequently, the catalytic performance can be ordered as follows: Au@D/TiO₂ > Au@G0/TiO₂ > Au@G1/TiO₂ > AuC/TiO₂ > Au@G2/TiO₂. These results evidence that longer dendron shells lead to lower catalytic activities, pointing to a balance between the number of Au nuclei and carbosilane dendrons/dodecanethiols. While the organic dendrons hinder gold aggregation due to the presence of carbosilane residues in the form of SiO₂ at the surface perimeter of Au NPs [18], an excess of SiO₂ has a negative effect on the performance of the PROX reaction, as in the case of Au@G2/TiO₂. A comparison of Au@D/TiO₂ and Au@G0/TiO₂ reveals that Au@D/TiO₂ showed superior catalytic activity under mixture B conditions and slightly higher activity for mixture C, despite the lower stability of Au@D/TiO₂ than Au@G0/TiO₂ supported on STO. Moreover, the catalysts derived from preformed Au NPs showed higher catalytic activity than the catalyst prepared using a conventional Au precursor for the three mixtures and temperatures tested, thus indicating that the dodecanethiol- and dendron-derived Au NPs lead to suitable PROX catalysts. It is worth noting here that the results of the TEM studies for Au@G1/TiO₂ and AuC/TiO₂ catalysts after calcination at 723 K showed that the mean particle size of Au@G1/TiO₂ was larger than for AuC/TiO₂. Thus, these results demonstrate that, for Au-based catalysts, it is not only the particle size that makes a major contribution to the catalytic performance, but other factors such as the Au-TiO₂ architecture or the chemical environment can determine their catalytic activity.

2.3.2. On Stainless Steel Microreactors

The best catalysts for PROX, namely Au@D/TiO₂ and Au@G0/TiO₂, and the reference catalyst, AuC/TiO₂, were tested in stainless steel microreactors.

Initially, a feed load test was carried out on the microreactor functionalized with Au@D/TiO₂. According to the results obtained on cordierite monoliths, to activate the catalysts, the reaction cycles started dosing mixture B at 473 K. Next, tests at increasing temperatures (363, 398, 433, and 473 K) were performed. The results for CO conversion are plotted in Figure 7 and the CO₂ selectivity in Figure S3. For both CO conversion and CO₂ selectivity, the expected trends were obtained: the lower the contact time, the lower the CO conversion and the higher the CO₂ selectivity, as previously reported [31]. For mixture B experiments in the low-temperature regime (363 and 398 K), CO₂ selectivity values higher than 90% were attained for all the gas hourly space velocities (GHSV) tested. For instance, at 398 K, up to $\chi_{CO} = 80\%$, associated with $S_{CO_2} = 94\%$, was attained. Full CO conversion was reached for the highest temperatures tested (433 and 473 K), obtaining, at 433 K, a CO₂ selectivity of 80%. In comparison to the operation of the catalyst supported on a cordierite monolith, the selectivity obtained under full conversion with the microreactor was higher than with the conventional monolith: at 433 K, $S_{CO_2} = 79\%$ (microreactor, $GHSV = 1.4 \times 10^4 \text{ h}^{-1}$) vs. $S_{CO_2} = 62\%$ (cordierite monolith) and at 473 K $S_{CO_2} = 74\%$ ($GHSV = 2.6 \times 10^4 \text{ h}^{-1}$) vs. $S_{CO_2} = 55\%$, which can be caused by the higher space velocities tested on microreactors and their better thermal management, since the catalytic layer is in direct contact with the metal platelets [32]. As expected, for all temperatures, a decrease in the CO conversion was observed under mixture C, except for 363 K, where similar values to those obtained for mixture B were recorded, as seen in Figure 7b. Both the CO conversion and the CO₂ selectivity followed a smooth variation for all the GHSV tested. Regarding CO oxidation experiments, for nearly all the space velocities, full CO conversion was reached at 473 K.

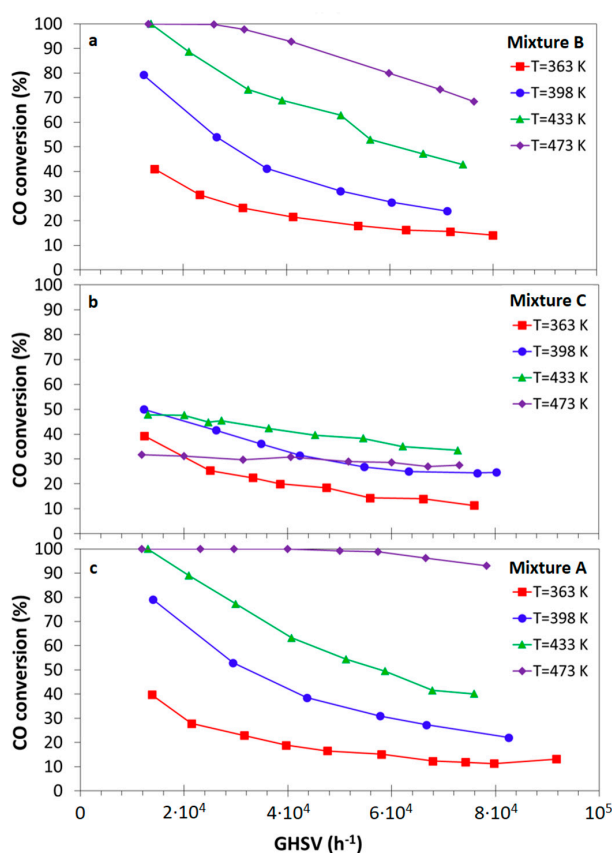


Figure 7. CO conversion for the feed load tests carried out for mixtures (a) B, (b) C, and (c) A tested on the microreactor functionalized with Au@D/TiO₂ catalyst.

The performance evaluation of microreactors loaded with Au@G0/TiO₂ and AuC/TiO₂ catalysts was carried out at the lowest GHSV (ca. $\text{GHSV} = 1.3 \times 10^4 \text{ h}^{-1}$). The CO conversion and CO₂ selectivity for both microreactors are presented in Figure 8. At the beginning of the experiments, low catalytic activity was recorded. Consequently, to improve the catalysts' performance and consonant with the XPS results, mixture B was dosed at increasing temperatures. This had a positive effect on the catalytic performance of Au@G0/TiO₂, which reached $\chi_{\text{CO}} = 82\%$ together with $S_{\text{CO}_2} = 85\%$ at 473 K after dosing mixture B at 773 K (Figure 8a). Under larger H₂ concentrations (mixture C experiments), at 363 and 398 K, similar CO conversions were obtained with lower CO₂ selectivities. However, for higher temperatures (433 and 473 K), both the CO conversion and CO₂ selectivity decreased, as the H₂ oxidation reaction took place to a larger extent. The CO oxidation activity also improved after dosing mixture B at increasing temperatures; nevertheless, for this microreactor, full CO conversion was not achieved. The maximum CO conversion, 94%, was recorded at 473 K.

The microreactor functionalized with the conventional Au catalyst (AuC/TiO₂) exhibited very low activity for all the conditions tested, with a CO conversion $\leq 10\%$ for the three mixtures in the 363–473 K temperature range. These results indicate that the preformed Au NPs are better Au precursors than the conventional HAuCl₄ to functionalize stainless steel microreactors, leading to superior catalytic performances. Comparing the performance of the three microreactors for mixture C, corresponding to a surrogate post-reformate stream, the highest CO conversion was achieved by the Au@D/TiO₂ catalyst, which converted up to 35 mL_{CO}/(min·g_{cat}) at 433 K and a spatial velocity of $7.3 \times 10^4 \text{ h}^{-1}$.

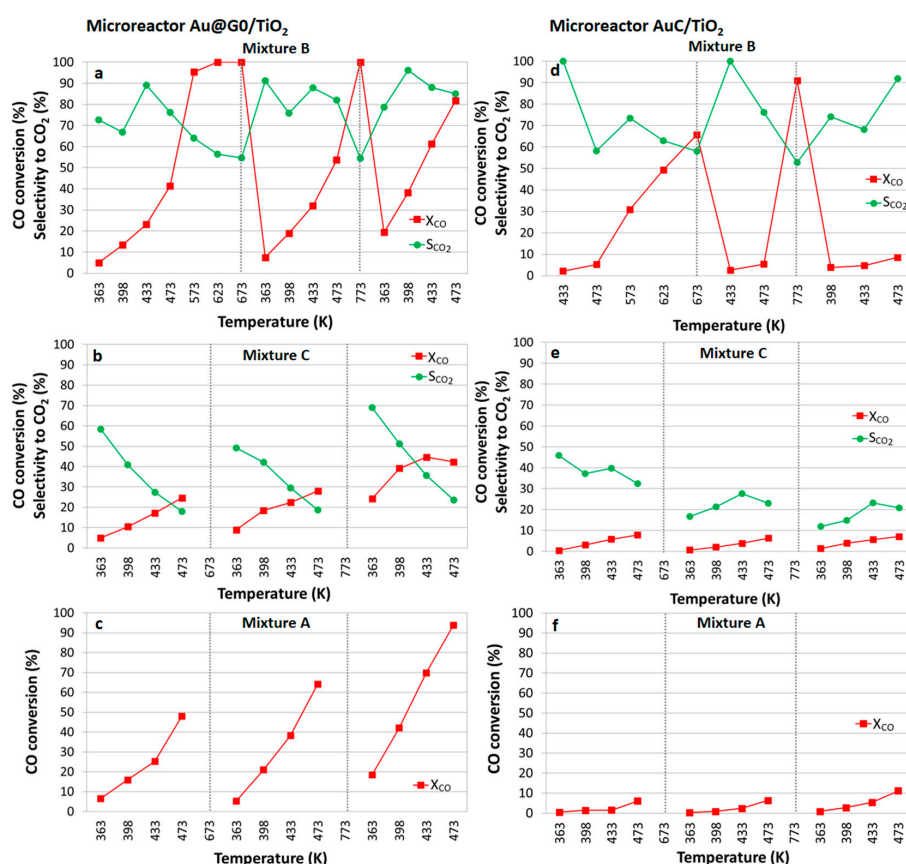


Figure 8. CO conversion and CO₂ selectivity as a function of temperature for the three reaction mixtures. (a–c) Au@G0/TiO₂ catalyst, and (d–f) AuC/TiO₂ loaded on stainless steel microreactors.

Finally, 500-hour stability tests were carried out, dosing a reformate surrogate at 453 K and evaluating the influence of CO₂ and steam. For these tests, Au@D/TiO₂ and Au@G0/TiO₂ catalysts supported on microreactors were chosen. The inlet concentration of the reactant mixture was

$\text{H}_2/\text{CO}/\text{O}_2/\text{N}_2/\text{CO}_2/\text{H}_2\text{O} = 48/0.85/0.85/3.3/18/29$. The same calcinations carried out for the previous tests on microreactors were performed and they were tested without further activation (see the Materials and Methods section for the calcination details). Figure 9a,b show the outlet species detected during the 500 h under operation for Au@D/TiO₂ and Au@G0/TiO₂, respectively. As seen in Figure 9a,b, the concentration of species at the outlet was stable during the whole test, indicating the remarkably stable operation of both catalysts during the 500 h. The corresponding CO conversion is plotted in Figure 9c. Initially, both microreactors showed a slight deactivation, but, after this period, they showed a stable performance without deactivation signs. No methane was detected. The conversion achieved during these tests was lower than for the previous tests. For instance, for Au@D/TiO₂, for mixture C, experiments at GHSV = $2.6 \times 10^4 \text{ h}^{-1}$, 45% and 30% CO conversion were obtained at 433 and 473 K, respectively, while a mean CO conversion of 24% was achieved during the stability test at 453 K, thus evidencing that the presence of CO₂ caused a reduction in the CO conversion. Nevertheless, our preformed Au@NCD/TiO₂ catalysts displayed a remarkably stable performance during the 500 h of stability tests under realistic reforming conditions, thus circumventing one of the major weaknesses identified for Au-based catalysts.

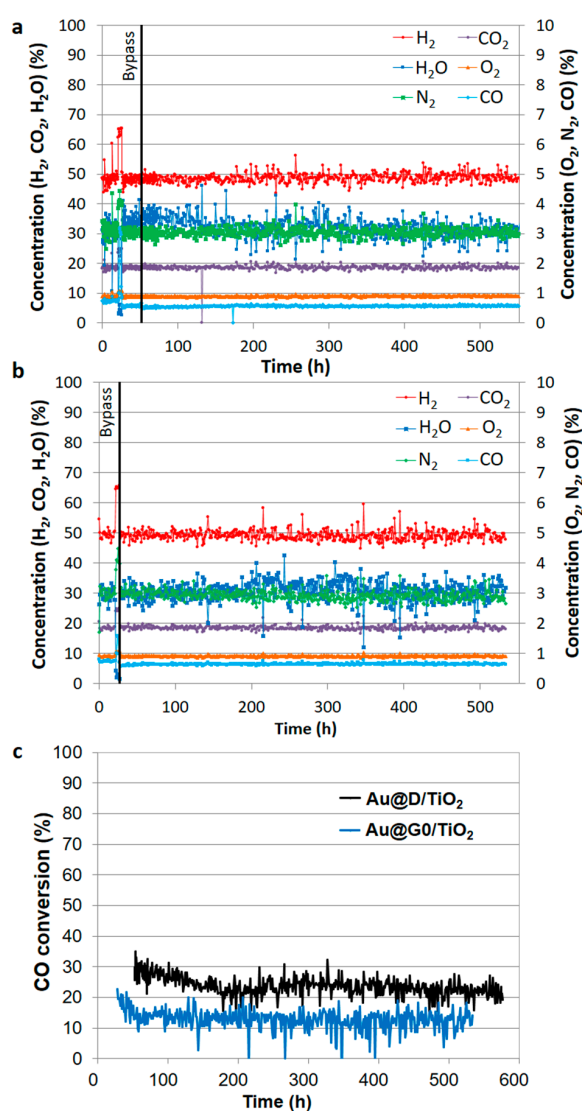


Figure 9. Long-term stability test performed at 453 K. Species detected at the outlet of (a) Au@D/TiO₂ and (b) Au@G0/TiO₂. (c) CO conversion for both microreactors. The concentration of the inlet mixture was measured for 20 h, which is the period marked as bypass.

3. Materials and Methods

3.1. Synthesis and Characterization of Au@NCD NPs

Four types of preformed Au NPs were synthesized, which consisted of Au cores stabilized with (i) dodecanethiols (D), and (ii) three different generations of trimethylsilane (TMS) dendrons functionalized in the focal point with a single thiol group, referred to as G0, G1, and G2 dendrons, as schematically represented in Figure 10. G0 dendrons contained only one TMS ramification, while G1 and G2 contained two and three TMS ramifications, respectively (Figure 10). The synthesis of the preformed Au NPs consisted of two steps: (1) synthesizing the thiol-functionalized ligands, whose synthesis details can be found in [25], and (2) the growing of metallic Au nuclei, while simultaneously attaching to them the self-assembled ligand monolayers following Brust's method [33]. Briefly, the synthesis details are as follows: tetractylammonium bromide (TOAB) was used to phase-transfer HAuCl_4 from aqueous solution to toluene. Next, the corresponding generation of previously synthesized dendrons was dissolved in toluene and added to the organic gold phase under vigorous stirring. Consequently, aqueous NaBH_4 was added with vigorous stirring as an Au^+ -reducing agent. During this process, while Au atoms were agglomerating, the different thiol-functionalized dendrons simultaneously attached to the growing Au nuclei, creating core-shell NPs. The synthesis procedure was repeated for the dodecanethiol-stabilized NPs and for the three dendron generations. The resulting dendron-encapsulated Au cores are referred to as Au@G0, for the Au cores encapsulated in G0 dendrons, and when encapsulated in G1 and G2 dendrons or dodecanethiols as Au@G1, Au@G2 and Au@D, respectively, as represented in Figure 10. The nomenclature of the Au NPs synthesized is summarized in Table 1.

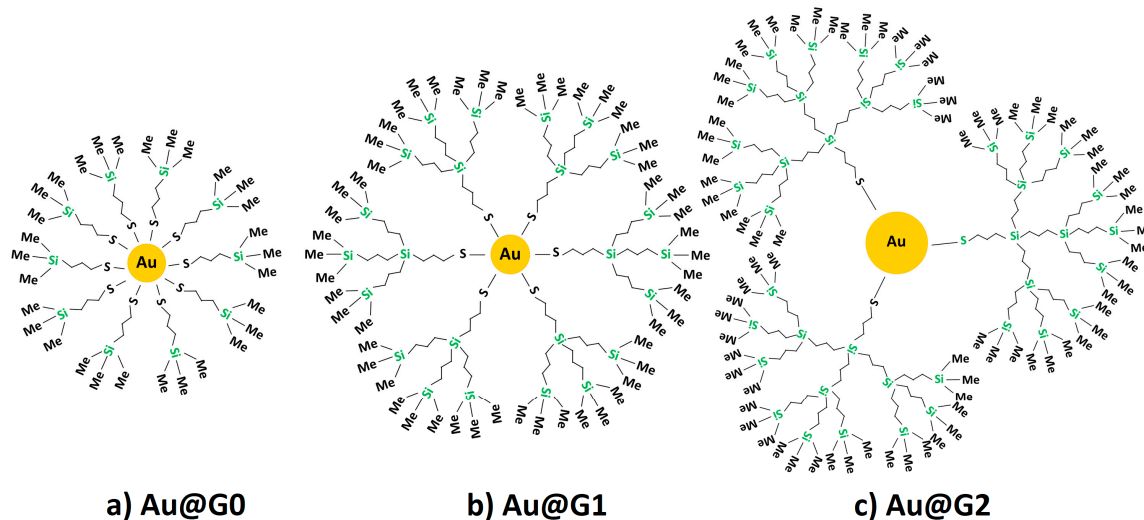


Figure 10. Scheme of the preformed Au NPs, consisting of a gold core encapsulated with (a) G0, (b) G1 and (c) G2 generation of trimethylsilane (TMS) dendrons.

The characterization of the synthesized Au@NCD was carried out by means of HRTEM, which was performed on a JEM 2010F from JEOL (Tokyo, Japan) electron microscope equipped with a field emission source at an accelerating voltage of 300 kV.

3.2. Synthesis and Characterization of TiO_2 Powder

Ti^{IV} isopropoxide ($\text{Ti}[\text{OCH}(\text{CH}_3)_2]_4$, >97%, Alfa Aesar) was dried out for 2 h at 393 K and then calcined for 4 h at 723 K (1 K/min).

The crystalline structure of the resulting powder was studied by X-ray diffraction, collecting diffractograms from 10° to 80° , at a step size of 0.02° and a step time of 1 s in an XRD diffractometer

(Bruker D8 Advance from Bruker, Germany) equipped with Ni-filtered (2 μm thickness) Cu K_{α} (Cu K_{α} = 1.5406 Å) radiation and operating at 40 KV and 40 mA.

Nitrogen adsorption isotherms were performed at 77 K using a Micromeritics ASAP2020 gas adsorption instrument. The materials were degassed at 473 K for 10 h prior to the adsorption experiments. Brunauer–Emmett–Teller (BET) and Barrett–Joyner–Halenda (BJH) models were applied to measure the surface area and mean pore diameter.

3.3. Functionalization and Characterization of Structured Reactors

3.3.1. Functionalization of Cordierite Honeycombs with Au/TiO₂ Catalysts

The catalytic tests were carried out on structured reactors. Two different supports were used, namely cordierite monoliths and stainless steel microreactors. The cordierite (2MgO·5SiO₂·2Al₂O₃) honeycombs used were of dimensions 1.8 × 1.8 × 1.8 cm³, containing 400 cells per square inch (cps) from Corning Celcor®. The functionalization started developing a TiO₂ layer on the cordierite honeycombs by immersing them in Ti^{IV} isopropoxide. Subsequently, the monoliths were dried out under continuous axial rotation at 353 K and at 393 K for 1 h. Next, they were calcined at 723 K for 4 h (2 K/min) (equivalent to the calcination treatment performed directly on the Ti^{IV} isopropoxide solution described above). Approximately 250 mg of TiO₂ coating was incorporated on the walls of the monolith's channels. Subsequently, by incipient wetness impregnation of the toluene solutions, the corresponding preformed Au NPs were deposited on the TiO₂-coated monoliths. The nominal gold metal loading for all samples was fixed at 2 wt.% of Au. Details of the calcination temperatures are given in the Results and Discussion section. Additionally, a monolith prepared using a conventional precursor (HAuCl₄·3H₂O, >97% Alfa Aesar) was also prepared for comparison purposes. A TiO₂-coated cordierite monolith was immersed in an ethanolic 0.012 M HAuCl₄·3H₂O (2wt.% Au) solution, which was subsequently dried out at 393 K for 2 h under axial rotation and then calcined at 723 K for 4 h (1 K/min). This catalyst is referred to as AuC/TiO₂.

The adherence of the TiO₂ coating to the channels' walls was checked by immersing in ethanol the TiO₂-coated cordierite monoliths and exposing them to ultrasounds (40 KHz) at increasing periods of time. After 9 min of ultrasound exposure, the TiO₂-coated monolith was dried at 353 K and weighed. The monolith lost ca. 5% of TiO₂, indicating that the TiO₂ layers developed from Ti^{IV} isopropoxide adhered well to the cordierite walls.

3.3.2. Functionalization of Stainless Steel Microreactors with Au/TiO₂ Catalysts

The stainless steel microreactors used were fabricated at the Mainz Institute of Microtechnology (IMM, Mainz, Germany). They consisted of two microstructured platelets laser-welded face to face, each of which contained 14 semicylindrical channels of 500- μm width, 250- μm depth, and 25-mm length. The microchannels were fabricated following a commercial photoetching process based on wet chemical etching with aqueous FeCl₃ [32]. Prior to welding the platelets, they were coated with TiO₂ anatase following a well-established procedure reported elsewhere [34]. Subsequently, the preformed Au NPs were anchored to the TiO₂ layer by adding the solutions containing preformed Au NPs dropwise to obtain a nominal 2 wt.% Au loading. Following this procedure, three microreactors were coated with Au@D/TiO₂, Au@G0/TiO₂ and AuC/TiO₂ catalysts. Figure S4 shows the inner part of the microchannels functionalized with the different Au/TiO₂ catalysts. The calcination temperature was chosen accordingly to the calcination temperatures that led to the best catalytic performance for each sample loaded on cordierite monoliths. Therefore, the microreactor loaded with Au@D/TiO₂ was calcined at 773 K (2 K/min) for 2 h; the microreactor loaded with Au@G0/TiO₂ at 673 K (2 K/min) for 2 h, and the one loaded with the conventional AuC/TiO₂ catalyst was calcined at 673 K (2 K/min) for 2 h, too. Once the platelets were loaded with the corresponding catalyst, they were welded and the inlet and outlet pipes were connected by laser-welding [35]. The sealing obtained by laser welding assured the leak tightness of the microreactors at operational temperatures up to 1023 K.

3.4. Synthesis of Unsupported Au/TiO₂ Catalysts

To be able to characterize the microstructure of the Au@NCD/TiO₂ catalysts developed on the walls of the structured supports, i.e., the cordierite monoliths and the microreactors, equivalent powdered Au@NCD/TiO₂ catalysts were synthesized. The Au@NCD/TiO₂ catalysts were prepared via incipient wetness impregnation of TiO₂, prepared from Ti^{IV} isopropoxide, with the solutions containing the different Au@NCDs to obtain a nominal 2 wt.% Au concentration. The Au@NCD/TiO₂ catalysts were calcined at 673 K for 2 h. Additionally, a 2 wt.% AuC/TiO₂ catalyst was prepared via incipient wetness impregnation of the TiO₂ powder with the conventional gold precursor (HAuCl₄·3H₂O, >97% Alfa Aesar). The resulting powder was calcined at 723 K for 2 h.

3.5. Characterization of Unsupported Au/TiO₂ Catalysts

XPS Analyses and XPS In Situ Measurements

To carry out XPS analyses, Si wafers were coated with TiO₂ anatase synthesized following the recipe used throughout this work, i.e., by using Ti^{IV} isopropoxide and calcining it at 723 K. Next, Au@D, Au@G1, and Au@G2 NPs were deposited by dropcasting the corresponding solutions of preformed Au@NCD and Keeping the same Au wt.%.

X-ray photoelectron spectroscopy (XPS) measurements were carried out in a SPECS (SPECS GmbH., Berlin, Germany) system equipped with an XR50 source, consisting of a twin Al/Mg anode and operated with the Al anode at 150 W, and a Phoibos MCD9 detector. The pass energy of the hemispherical analyzer was set to 25 eV and the energy step was set to 0.1 eV. The thermal treatments were performed directly inside the analysis chamber and the base pressure to acquire XPS spectra was kept at 10⁻⁷ bar. Data processing was performed using the CasaXPS program (Casa Software Ltd.). The binding energies were calibrated for energy using the adventitious C 1s signal at 284.8 eV.

The series of in situ treatments was performed on a high-pressure cell (HPC) connected to the XPS system. For these experiments, a pellet of 10 wt.% Au@G0/TiO₂ was prepared and introduced in the XPS setup after drying it for 10 min with an infrared lamp. A higher Au loading was chosen to obtain a higher resolution for Au. The series of in situ treatments consisted of an oxidation with 20 mL/min of air for 10 min at: (i) 473 K, (ii) 573 K, (iii) 673 K, (iv) a PROX atmosphere at 673 K dosing 3 mL/min CO + 3 mL/min H₂ + 15 mL/min air (mixture B-like conditions), (v) oxidation at 773 K, (vi) and oxidation at 873 K. The deconvolution of gold 4f spectra was performed following the spin-orbit constraints, i.e., forcing the distance between Au4f_{7/2} and Au4f_{5/2} components at 3.67 eV [26] and the ratio between their areas. The spin-orbit constraints for area and binding energy were also kept for the deconvolution of Ti 2p. All spectra were calibrated for energy, taking as a reference the adventitious C 1s signal at 284.8 eV.

3.6. CO Oxidation and PROX Catalytic Tests

Three gaseous mixtures were dosed to investigate the performance of the catalysts, which contained CO and O₂ at a fixed molar ratio of one and different H₂ concentrations, as presented in Table 4.

Independent mass flow controllers (M + W Instruments) were used to dose the reactant mixtures under atmospheric pressure. Mixture A experiments corresponded to CO total oxidation tests, while 50 vol.% H₂ was present, as in post-reformate streams, in mixture C, thus containing a realistic amount of H₂. The O₂/CO molar ratio was fixed at 1 ($\lambda = 2$, Equation (1)), since it represents an optimum value, balancing CO oxidation activity and selectivity [31]. Typically, in the off-gas of water-gas shift (WGS) reactors, CO concentrations range between 0.5 and 2 vol.%. Therefore, in our experiments, the CO concentration was fixed at 2 vol.% (the upper limit), representing the most unfavorable scenario. An online analysis of reaction products was carried out every 5 min using a gas micro-chromatograph (Agilent 3000A) equipped with MS 5Å, Plot U, Stabilwax capillary columns and thermal conductivity detectors (TCD). The experimental error is ca. 5% for all experiments.

The O₂/CO molar ratio, CO conversion, O₂ conversion, and selectivity towards CO₂ formation were calculated according to Equations (1)–(4), respectively:

$$\lambda = 2 \frac{\dot{n}_{O_2}}{\dot{n}_{CO}} \quad (1)$$

$$\chi_{CO} = \frac{\dot{n}_{CO,in} - \dot{n}_{CO,out}}{\dot{n}_{CO,in}} 100, \text{ where } [\dot{n}] = \frac{mol}{s} \quad (2)$$

$$\chi_{O_2} = \frac{\dot{n}_{O_2,in} - \dot{n}_{O_2,out}}{\dot{n}_{O_2,in}} 100 \quad (3)$$

$$S_{CO_2} = \frac{\dot{n}_{CO,in} - \dot{n}_{CO,out}}{(\dot{n}_{CO,in} - \dot{n}_{CO,out}) + (\dot{n}_{H_2,in} - \dot{n}_{H_2,out})} 100 \quad (4)$$

3.6.1. On Cordierite Monoliths

To test the functionalized cordierite monoliths, they were fitted inside stainless steel tubular reactors (21 mm internal diameter). The loaded reactors were introduced in a tubular furnace (Carbolite) controlled by a proportional–integral–derivative (PID) controller (Fuji PXR4). A total inlet flow of 100 mL/min was kept for the three mixtures, corresponding to GHSV = $1.3 \times 10^3 \text{ h}^{-1}$. After each reaction cycle with the three mixtures (B, A, C) at 363, 398, 433, and 473 K, an oxidation with synthetic air (20 vol.% O₂ balanced in N₂) was performed for 1 h at increasing temperatures. This was done to find the optimum combination of activation treatments. Ramp rates of 5 K/min were used to increase/decrease the temperature. The reaction cycle is schematically represented in Figure S1.

3.6.2. On Stainless Steel Microreactors

The microreactors were tested on the same experimental setup, where the inlet flow of reactants was regulated by a needle valve. The feed loads investigated on the Au@D/TiO₂ catalyst represented GHSV between 1.2×10^4 and $9.2 \times 10^4 \text{ h}^{-1}$, corresponding to weight hourly space velocities (WHSV) ranging from 52,400 to 390,200 mL/(h·g_{cat}) (considering the volume of the 14 microchannels).

3.6.3. Long-Term Test

Two freshly functionalized microreactors with Au@D/TiO₂ and Au@G0/TiO₂ catalysts were used to investigate the influence of a real post-reformate stream at 453 K and atmospheric pressure for 500 h. The total inlet flux was fixed at 30 mL/min, corresponding to a GHSV = $2.6 \times 10^4 \text{ h}^{-1}$. The composition of the inlet mixture was as follows: H₂/CO/O₂/N₂/CO₂/H₂O = 48.0/0.85/0.85/3.3/18/29. The inlet mixture concentration was monitored for 20 h to ensure a stable injection throughout the 500-h test. This period of time is marked in Figure 9 with the word bypass.

4. Conclusions

Gold NPs stabilized with dodecanethiols and G0 dendrons showed the highest thermal stability upon oxidation at different temperatures. The catalysts supported on cordierite monoliths showed a catalytic performance for a mixture containing 2 vol.% CO, 2 vol.% O₂ and 50 vol.% H₂ (balanced in Ar) that can be ordered as follows: Au@D/TiO₂ > Au@G0/TiO₂ > Au@G1/TiO₂ > Au@C/TiO₂ > Au@G2/TiO₂, thus showing that the preformed Au NPs lead to suitable catalysts for the PROX reaction. Au@D/TiO₂ catalysts exhibited the best performance when supported on stainless steel microreactors as well, outperforming a catalyst synthesized using a conventional HAuCl₄ salt. Therefore, using preformed Au NPs is an effective method for the synthesis of Au/TiO₂ catalysts. For mixtures containing 2 vol.% H₂, 2 vol.% CO, 2 vol.% O₂, the Au@D/TiO₂ on the microreactor attained full CO conversion at the lower spatial velocities tested and CO₂ selectivities higher than 90% at 363 and 398 K were reached

for all contact times. During the stability tests performed on microreactors loaded with Au@D/TiO₂ and Au@G0/TiO₂ catalysts under a reformat surrogate stream containing 18 vol.% CO₂ and 29 vol.% H₂O, the stable operation of both catalysts was observed for 500 h, thus demonstrating the stable operation of our ligand-derived Au catalysts. An average CO conversion of 24% was achieved during these tests.

Supplementary Materials: The following are available online at <http://www.mdpi.com/2073-4344/10/9/1028/s1>, Figure S1: Sequence of experimental conditions performed, highlighting the order of the reaction mixtures, temperatures and details of the oxidations performed. Figure S2: Temperature dependence performance of (a) Au@D/TiO₂, (b) Au@G0/TiO₂, (c) Au@G1/TiO₂, and (d) AuC/TiO₂ catalysts for mixture A. Black vertical lines in (a–c) indicate the oxidations performed; grey lines in (d) show when mixture B was dosed at a higher temperature. Figure S3: CO₂ selectivity for the feed load tests carried out for mixtures B and C on the microreactor functionalized with Au@D/TiO₂. Figure S4: Upper photographs: Detail of the inner part of the microreactors showing the microchannels coated with TiO₂ and three different Au precursors: Au@D, Au@G0, and HAuCl₄·3H₂O. Lower photograph: detail of an assembled microreactor. The scale is shown in cm.

Author Contributions: Conceptualization, N.J.D., J.L.; methodology, N.J.D., J.L.; validation, N.J.D., E.L., G.K., J.L.; investigation, N.J.D.; E.L.; R.Z. microchannel coating; S.N. long term activity tests; I.A. synthesis of preformed Au NPs; writing—original draft preparation, N.J.D.; writing—review and editing, N.J.D., E.L., I.A., G.K., J.L.; supervision, J.L.; funding acquisition, G.K., J.L. All authors have read and agreed to the published version of the manuscript.

Funding: This work was supported by projects from the Spanish Ministerio de Ciencia e Innovación MICINN/FEDER RTI2018-093996-B-C31 and Generalitat de Catalunya (GC) 2017 SGR 128. NJD received funding from the postdoctoral fellowships programme Beatriu de Pinós (2018 BP 00146), funded by the Secretary of Universities and Research (Government of Catalonia) and by Horizon 2020 programme of research and innovation of the European Union under the Marie Skłodowska-Curie grant agreement No 801370. JL is a Serra Hünter Fellow and is grateful to the ICREA Academia program.

Conflicts of Interest: The authors declare no conflict of interest.

References

1. Gandía, L.M.; Arzamendi, G.; Diéguez, P.M. Renewable Hydrogen Energy: An Overview. In *Renewable Hydrogen Technologies: Production, Purification, Storage, Applications and Safety*; Elsevier B.V.: Amsterdam, The Netherlands, 2013; pp. 1–17.
2. Haryanto, A.; Fernando, S.; Murali, N.; Adhikari, S. Current Status of Hydrogen Production Techniques by Steam Reforming of Ethanol: A Review. *Energy Fuels* **2005**, *19*, 2098–2106. [[CrossRef](#)]
3. Choudhary, T. CO-free fuel processing for fuel cell applications. *Catal. Today* **2002**, *77*, 65–78. [[CrossRef](#)]
4. Korotkikh, O.; Farrauto, R.J. Selective catalytic oxidation of CO in H₂: Fuel cell applications. *Catal. Today* **2000**, *62*, 249–254. [[CrossRef](#)]
5. Liu, K.; Wang, A.; Zhang, T. Recent Advances in Preferential Oxidation of CO Reaction over Platinum Group Metal Catalysts. *ACS Catal.* **2012**, *2*, 1165–1178. [[CrossRef](#)]
6. Choi, Y.; Stenger, H.G. Kinetics, simulation and insights for CO selective oxidation in fuel cell applications. *J. Power Sources* **2004**, *129*, 246–254. [[CrossRef](#)]
7. Pozdnyakova, O.; Teschner, D.; Woosch, A.; Krohnert, J.; Steinhauer, B.; Sauer, H.; Tóth, L.; Jentoft, F.; Knopgericke, A.; Paal, Z. Preferential CO oxidation in hydrogen (PROX) on ceria-supported catalysts, part I: Oxidation state and surface species on Pt/CeO₂ under reaction conditions. *J. Catal.* **2006**, *237*, 1–16. [[CrossRef](#)]
8. Haruta, M. Size- and support-dependency in the catalysis of gold. *Catal. Today* **1997**, *36*, 153–166. [[CrossRef](#)]
9. Haruta, M. Gold as a novel catalyst in the 21st century: Preparation, working mechanism and applications. *Gold Bull.* **2004**, *37*, 27–36. [[CrossRef](#)]
10. Valden, M.; Lai, X.; Goodman, D.W. Onset of Catalytic Activity of Gold Clusters on Titania with the Appearance of Nonmetallic Properties. *Science* **1998**, *281*, 1647–1650. [[CrossRef](#)]
11. Chen, M.; Goodman, D.W. Catalytically Active Gold: From Nanoparticles to Ultrathin Films. *Accounts Chem. Res.* **2006**, *39*, 739–746. [[CrossRef](#)]
12. Lopez, N. On the origin of the catalytic activity of gold nanoparticles for low-temperature CO oxidation. *J. Catal.* **2004**, *223*, 232–235. [[CrossRef](#)]

13. Beck, A.; Yang, A.-C.; Leland, A.R.; Riscoe, A.R.; Lopez, F.A.; Goodman, E.D.; Cargnello, M. Understanding the preferential oxidation of carbon monoxide (PrOx) using size-controlled Au nanocrystal catalyst. *AIChE J.* **2018**, *64*, 3159–3167. [[CrossRef](#)]
14. Chen, M.; Goodman, D.W. Catalytically active gold on ordered titania supports. *Chem. Soc. Rev.* **2008**, *37*, 1860–1870. [[CrossRef](#)] [[PubMed](#)]
15. Qiao, B.; Liu, J.; Wang, Y.-G.; Lin, Q.; Liu, X.; Wang, A.; Li, J.; Zhang, T.; Liu, J. Highly Efficient Catalysis of Preferential Oxidation of CO in H₂-Rich Stream by Gold Single-Atom Catalysts. *ACS Catal.* **2015**, *5*, 6249–6254. [[CrossRef](#)]
16. Llorca, J.; Domínguez, M.; Ledesma, C.; Chimentao, R.J.; Medina, F.; E Sueiras, J.; Angurell, I.; Seco, M.; Rossell, O. Propene epoxidation over TiO₂-supported Au–Cu alloy catalysts prepared from thiol-capped nanoparticles. *J. Catal.* **2008**, *258*, 187–198. [[CrossRef](#)]
17. Divins, N.J.; López, E.; Roig, M.; Trifonov, T.; Rodriguez, A.; De Rivera, F.G.; Rodríguez, L.; Seco, M.; Rossell, O.; Llorca, J. A million-channel CO-PrOx microreactor on a fingertip for fuel cell application. *Chem. Eng. J.* **2011**, *167*, 597–602. [[CrossRef](#)]
18. Moreno, C.; Divins, N.J.; Gázquez, J.; Varela, M.; Angurell, I.; Llorca, J. Improved thermal stability of oxide-supported naked gold nanoparticles by ligand-assisted pinning. *Nanoscale* **2012**, *4*, 2278. [[CrossRef](#)]
19. Soler, L.; Casanovas, A.; Urrich, A.; Angurell, I.; Llorca, J. CO oxidation and COPrOx over preformed Au nanoparticles supported over nanoshaped CeO₂. *Appl. Catal. B Environ.* **2016**, *197*, 47–55. [[CrossRef](#)]
20. Cominos, V.; Hessel, V.; Hofmann, C.; Kolb, G.; Zapf, R.; Ziogas, A.; Delsman, E.; Schouten, J. Selective oxidation of carbon monoxide in a hydrogen-rich fuel cell feed using a catalyst coated microstructured reactor. *Catal. Today* **2005**, *110*, 140–153. [[CrossRef](#)]
21. Potemkin, D.; Snytnikov, P.; Belyaev, V.; Sobyenin, V. Preferential CO oxidation over Cu/CeO_{2-x} catalyst: Internal mass transport limitation. *Chem. Eng. J.* **2011**, *176*, 165–171. [[CrossRef](#)]
22. Soler, L.; Divins, N.J.; Vendrell, X.; Serrano, I.; Llorca, J. Hydrogen production in microreactors. In *Current Trends and Future Developments on (Bio-) Membranes*; Elsevier: Amsterdam, The Netherlands, 2020; pp. 141–182.
23. Leal, G.B.; Ciotti, L.; Watacabe, B.N.; Da Silva, D.C.L.; Antoniassi, R.M.; Silva, J.C.M.; Linardi, M.; Giudicci, R.; Vaz, J.M.; Spinacé, E.V. Preparation of Au/TiO₂ by a facile method at room temperature for the CO preferential oxidation reaction. *Catal. Commun.* **2018**, *116*, 38–42. [[CrossRef](#)]
24. Ivanova, S.; Pitchon, V.; Petit, C.; Caps, V. Support Effects in the Gold-Catalyzed Preferential Oxidation of CO. *ChemCatChem* **2010**, *2*, 556–563. [[CrossRef](#)]
25. De Rivera, F.G.; Rodríguez, L.-I.; Rossell, O.; Seco, M.; Divins, N.J.; Casanova, I.; Llorca, J. Carbosilane dendrons as stabilizing agents for the formation of gold nanoparticles. *J. Organomet. Chem.* **2011**, *696*, 2287–2293. [[CrossRef](#)]
26. Wagner, C.D.; Riggs, W.M.; Davis, L.E. *Handbook of X-Ray Photoelectron Spectroscopy*; PerkinElmer: Waltham, MA, USA, 1979.
27. Schubert, M.M.; Plzak, V.; Garche, J.; Behm, R.J. Activity, Selectivity, and Long-Term Stability of Different Metal Oxide Supported Gold Catalysts for the Preferential CO Oxidation in H₂-Rich Gas. *Catal. Lett.* **2001**, *76*, 143–150. [[CrossRef](#)]
28. Laguna, O.; Ngassa, E.; Oraá, S.; Alvarez, A.; Domínguez, M.; Romero-Sarria, F.; Arzamendi, G.; Gandía, L.M.; Centeno, M.A.; Odriozola, J.A.; et al. Preferential oxidation of CO (CO-PROX) over CuOx/CeO₂ coated microchannel reactor. *Catal. Today* **2012**, *180*, 105–110. [[CrossRef](#)]
29. Widmann, D.; Hocking, E.; Behm, R. On the origin of the selectivity in the preferential CO oxidation on Au/TiO₂—Nature of the active oxygen species for H₂ oxidation. *J. Catal.* **2014**, *317*, 272–276. [[CrossRef](#)]
30. Green, I.X.; Tang, W.; Neurock, M.; Yates, J.T. Spectroscopic Observation of Dual Catalytic Sites During Oxidation of CO on a Au/TiO₂ Catalyst. *Science* **2011**, *333*, 736–739. [[CrossRef](#)]
31. Reina, T.R.; Ivanova, S.; Centeno, M.A.; Odriozola, J.A. Catalytic screening of Au/CeO₂-MO_x/Al₂O₃ catalysts (M = La, Ni, Cu, Fe, Cr, Y) in the CO-PrOx reaction. *Int. J. Hydrogen Energy* **2015**, *40*, 1782–1788. [[CrossRef](#)]
32. Snytnikov, P.; Popova, M.; Men, Y.; Rebrov, E.; Kolb, G.; Hessel, V.; Schouten, J.; Sobyenin, V. Preferential CO oxidation over a copper–cerium oxide catalyst in a microchannel reactor. *Appl. Catal. A Gen.* **2008**, *350*, 53–62. [[CrossRef](#)]
33. Brust, M.; Walker, M.; Bethell, D.; Schiffrin, D.J.; Whyman, R. Synthesis of thiol-derivatised gold nanoparticles in a two-phase Liquid-Liquid system. *J. Chem. Soc. Chem. Commun.* **1994**, 801–802. [[CrossRef](#)]

34. Zapf, R.; Becker-Willinger, C.; Berresheim, K.; Bolz, H.; Gnaser, H.; Hessel, V.; Kolb, G.; Löb, P.; Pannwitt, A.-K.; Ziogas, A. Detailed Characterization of Various Porous Alumina-Based Catalyst Coatings Within Microchannels and Their Testing for Methanol Steam Reforming. *Chem. Eng. Res. Des.* **2003**, *81*, 721–729. [[CrossRef](#)]
35. O’Connell, M.; Kolb, G.; Zapf, R.; Men, Y.; Hessel, V. Bimetallic catalysts for the catalytic combustion of methane using microreactor technology. *Catal. Today* **2009**, *144*, 306–311. [[CrossRef](#)]



© 2020 by the authors. Licensee MDPI, Basel, Switzerland. This article is an open access article distributed under the terms and conditions of the Creative Commons Attribution (CC BY) license (<http://creativecommons.org/licenses/by/4.0/>).